Development of an enhanced burr accumulation model during orthogonal cutting of nickel-based super alloy

Côme Legrand[1,2] · Guillaume Fromentin[1] · Gérard Poulachon[1] · Mickael Rancic[2]

Abstract
Burr size is a real issue in aeronautic for machining highly critical parts, such as broaching of turbine disks, it may affect the mechanical resistance of the part. However, the analysis and modelling of the burr formation and its accumulation is challenging due to the small concerned root area and the change of its shape after multiple cuts. In the state of the art, there is not much contribution on the burr mechanism during accumulation. To investigate this subject on nickel-based super alloy parts, an experiment with an in situ camera and LASER profilometer has been developed to follow the burr growth after multiple passes. Then, a phenomenological model of burr accumulation is formulated based on the description of a plastic hinge appearance during burr formations. It enables the modelling of burr height, root thickness and added material to the burr after each pass. Burr fracture occurrence is also discussed. This work proposes a new outlook on the burr formation mechanism and complete the models previously developed in the known literature.

Keywords Burr modelling · Burr accumulation · Planing experiment · Burr measurements

1 Introduction

The modelling of burrs formation is a real issue on critical parts. In the industry, it is necessary to remove them for insuring fatigue resistance. These deburring operations induce extra costs, explaining the need of reliable models to minimize burrs size. This study focuses on two types of exit burrs. They are presented on Fig. 1 and named according to Régnier et al. [1]. The first type corresponds to burrs without chamfer (cf. Fig. 1a). They are described by Gillespie and Blotter [2] as the long ones found at the end of a cut. During a broaching operation, cut thickness is usually small and often smaller than the root thickness of the burrs without chamfer. This configuration may lead to burr accumulation according to Régnier et al. [3]. Thus, the large number of teeth on a broach could conduct to a situation where each tooth, one after the other, pushes the matter outside of the part, resulting in a burr growth by accumulation. The second type of burrs, which is discussed in the last part of this article, concerns burr with chamfer (cf. Fig. 1b) resulting of a crack propagation while the tool moves outside of the workpiece, preventing a burr without chamfer to be shaped.

Hashimura et al. [4] describe the steps of burr formation and the critical moment when a crack may initiate or not to form a burr with or without chamfer for one cut. According to the authors, the type of burr depends on the work material behaviour: ductile (without chamfer burrs) or fragile (with chamfer burrs). Their observations are done at very low speed (25 µm/s) in a scanning electron microscope (SEM) during copper and Al-2024-O aluminium alloy machining. A finite element analysis based on their observations is presented in parallel to give results that could help the development of future mechanical models. Régnier et al. [5] observe during the machining of a cast aluminium alloy (AlSi7Mg0.3 + 0.5Cu) that both types of burr may appear on the same part exit edge due to the microstructure heterogeneity and that the proportion of the burr type can be controlled by changing the cut thickness in orthogonal cutting. Olvera and Barrow [6] explain also that the axial depth of cut in milling can change the type of burr and that it exists a transition value of the cut thickness parameter. Low cut thickness is associated with burr without chamfer, and high ones with the

✉ Côme Legrand
come.legrand@ensam.eu

[1] Arts Et Metiers Institute of Technology, LABOMAP, Université Bourgogne Franche-Comté, HESAM Université, F-71250 Cluny, France

[2] Safran Aircraft Engines, Rue Henri Auguste Desbruères, F-91000 Évry, France

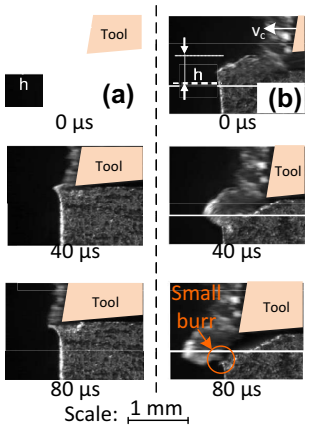

Fig. 1 Burr types observed in a cast aluminium alloy (AlSi7Mg0.3+0.5Cu) with a high-speed CCD camera PHOTRON SA–Z. **a** Burr without chamfer (h=0.03 mm, γ=7°). **b** Burr with chamfer (h=0.1 mm, γ=7°). Adapted from Régnier et al. [3]

other type. According to observations, a small burr (circled in Fig. 1b) may appear at the end of the crack propagation area after the formation of a burr with chamfer.

Aurich et al. [7] show in their bibliography review that the main parameters that influence burr formation are work material, tool geometry, wear, machining parameters (especially cut thickness and cutting speed), and shape of the workpiece at tool exit. The three first parameters are also very influent on cutting forces. Several studies [8–10] introduce burr geometrical models based on cutting force or their mechanistic formulation. Such modelling approach shows good results but does not consider the mechanic of burr formation and only gives results for one output.

Few mechanical models exist to describe the burr formation during orthogonal cutting in the known literature. They are based on the plastic hinge theory.

Ko and Dornfeld [11] introduce a model of burr formation based on observations of plasticine and copper machining, two ductile materials, at very low speed. These observations lead to distinguish three steps during burr formation:

(i) Burr formation initiation. When the tool reaches the part exit edge, there is a point (A) where the chip stops growing and the burr formation starts (cf. Fig. 2a). Pekelharing [12] also observe this phenomenon in AISI 1045 steel. The tool cutting edge is then at a distance w of the part exit surface. At this point, the energy previously used to generate the chip, now develops the burr. The previous positive shear plane at the chip root is transformed to a negative shear plane at an angle β_0 with the machined surface. It starts at the tool tip and finishes at a point, which becomes the centre of a plastic hinge (B), at the part exit surface.

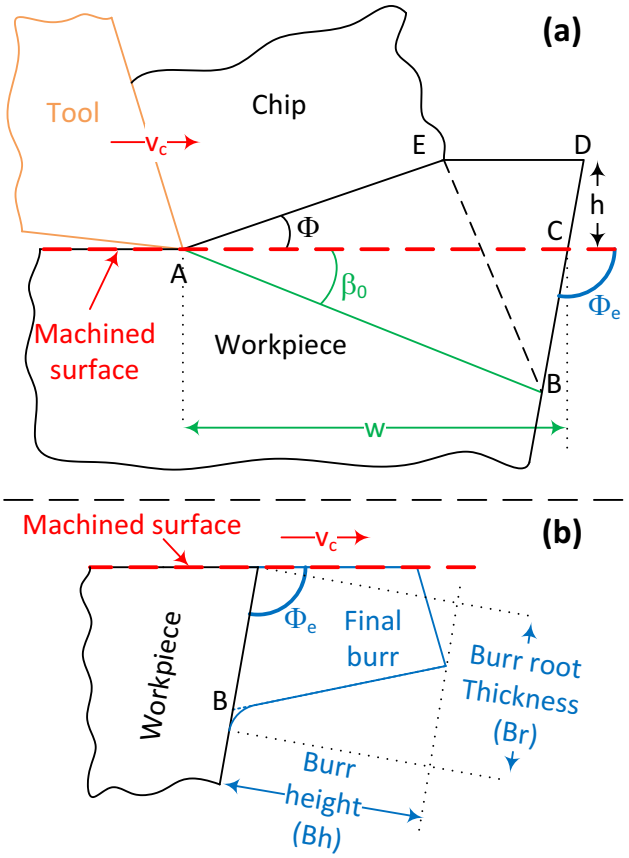

Fig. 2 Description of **a** the burr at the initiation step and **b** the shape of the final burr

(ii) Burr development. As the tool moves forward, the negative shear plane rotates, the plastic hinge centre staying at the same position. The material above this plane is considered to rotate. The maximal strain is supposed to be at the tool tip. The deformation is composed of plastic shear and bending.

(iii) Burr formation. The burr is shaped by the rotation of the negative deformation plane that pushes the material outside of the part. As the plane rotates, the strain increases. If a fracture occurs, it will propagate along the negative deformation plane and create a burr with chamfer. The modelling of crack initiation for burr with chamfer is discussed in a following paragraph. Figure 2b introduces the final burr shape description that is used in this article.

Ko and Dornfeld [11] determine w and β_0 considering the minimum energy principle and the energy conservation. In addition, Ko and Dornfeld [13] introduce the effect of the tool cutting edge inclination angle into their previous burr model.

Chern and Dornfeld [14] use the same approach for the burr formation description but introduce the hypothesis of

the incompressibility of the triangles ABC and BCE. This methodology for the β_0 calculation is assumed to be more accurate than the one proposed in [11]. They also introduce the influence of the part exit angle Φ_e. The results are in good agreement with experimental measurements for copper and two aluminium alloys.

Toporov et al. [15] describe the 2D negative deformation curve not with a straight line but with a slip line that have the shape of an arc of a circle. The burr incompressibility hypothesis is also used. The results are in agreement with experimental observations for pure copper. The model also takes into account the tool exit angle Φ_e.

Niknam and Songmene [16] use a similar mechanical model, as the one described in [11], to predict burr thickness when milling two aluminium alloys. They show good agreements between experimental results and calculated values in an operation which is not planning.

To conclude, a high link between chip and burr formation exists. The mechanical modelling of burr formation seems to be relevant with experimental results close to modelled values in ductile materials. The key parameters appear to be cut thickness, cutting forces, chip shear angle and tool exit angle.

The present study focuses on the understanding and the modelling of burr formation and its accumulation after multicut. The configuration used is orthogonal cutting of nickel based alloy. A novel geometrical approach of burr formation is proposed considering the burr accumulation process. The developed methodology based on a plastic hinge mechanical model allows the quantification of burr height, root thickness and added volume by each cut, during accumulation. The effect of the cutting geometry, the cut thickness and the orientation of the part exit surface is discussed thanks to an experiment developed to follow after several cuts the burr growth with an in situ camera and a LASER profilometer. The model has been extended to evaluate the occurrence of crack initiation leading to burr with chamfer. This work proposes a new outlook on the burr formation mechanism and complete the models already developed in the known literature.

2 Experimental setup and measurements

2.1 Experimental setup and parameters

The experimental setup is presented on Fig. 3. It allows carrying out a planing operation in a 3-axes gantry milling machine DMG DMC-85 V along its X-axis. The moving sample is maintained in a holder which is attached to the

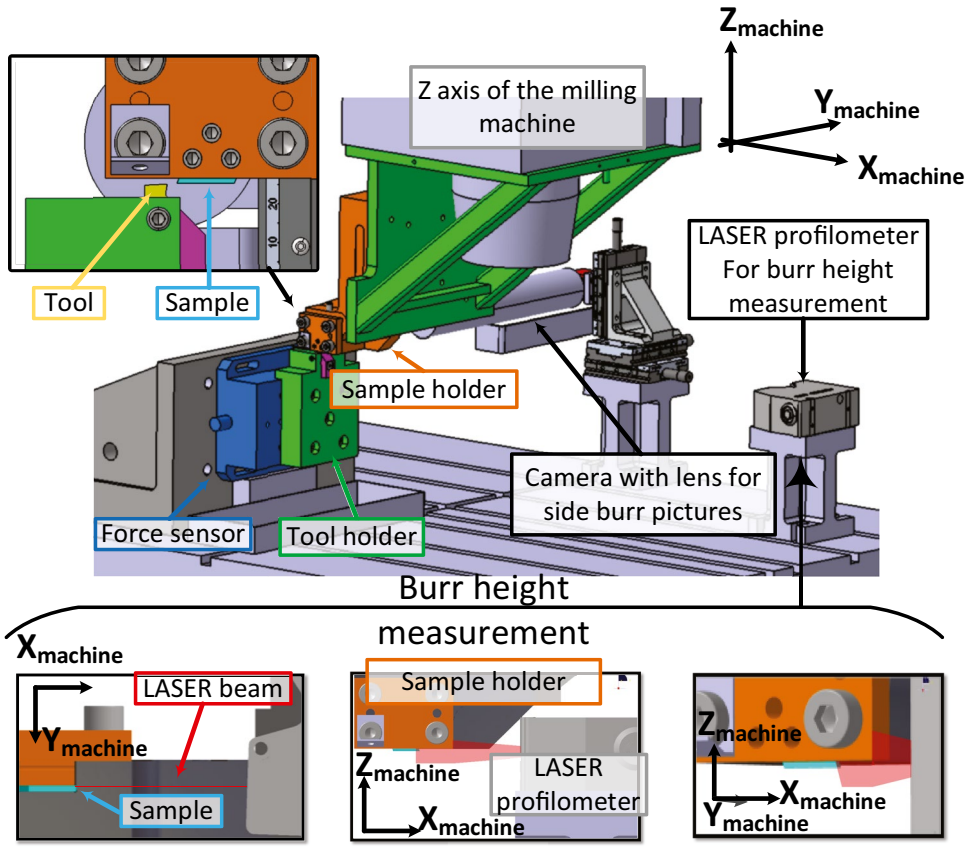

Fig. 3 Experimental setup for burr and chip analysis

Z-axis of the milling machine. The tool stays fixed in the machine environment and is attached to a tool holder located on a Kistler 9257 force sensor. It measures the cutting forces during the planing operations in the three axes (X, Y, Z) of the milling machine. A Basler acA19210-155um camera is used to capture a picture of the burr side after a planing cut. It has a 2.3 MP CMOS sensor. A telecentric lens is added to the camera to limit optical aberrations. The camera axis is parallel to the Y machine axis. In addition, a LJ-V7060 Keyence LASER profilometer located on the machine table allows scanning the burr shape, all along the sample exit edge. The LASER beam located in the XZ machine plane has a measurement repeatability of 0.4 µm and 5 µm along the X and Z axes respectively. The third scan direction is obtained by moving the sample with the Y-axis, and the linear encoder of the machine is used to trig the LASER profilometer every 4 µm increment.

This experimental setup allows to characterise the burr geometry between each cut, and then to evaluate its accumulation. The capture of the burr side picture and the burr scan takes time, so it only has been recorded for some selected cut numbers.

The experimental procedure is the following one:

(i) Scan with the LASER profilometer of the initial sample exit surface before any cut,
(ii) Single planing operation with forces measurement,
(iii) Capture of the burr profile picture with the camera, in the case of the selected cut,
(iv) Three dimensional scan of the burr at the sample exit edge, in the case of the selected cut,
(v) Go back to ii for a new cut.

It appears this first global scan of the burr is contaminated by some non-consistent points, mainly due to the sharp edges of the sample and the reflections on its holder. The first step of the process presented on Fig. 4a consists of deleting these points to clean the scans.

On Fig. 4b, a best-fit plane is determined thanks to the point cloud of the initial surface scan of the sample before the 1st cut. This plane becomes the reference for the next analyses, with its own coordinate system.

One hundred consecutive profiles, in the $XZ_{machine}$ plane, are extracted from the centre part of each burr scan and then rotated in the reference exit plane coordinates system. Figure 4c shows a graph where the one hundred selected profiles are in the exit plane coordinates system. The point having the maximum altitude (along the $Z_{exit\ plane}$ axis) determines the burr height for each profile. The mean value and the standard deviation of the one hundred local burr heights are then calculated and plotted on a graph, as on Fig. 4d. This graph shows the burr height as a function of the accumulated cut thickness and presents the results of the burr

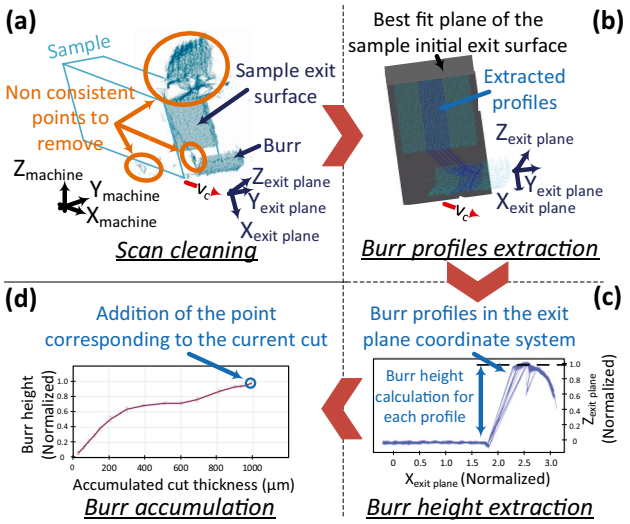

Fig. 4 Analysis methodology for burr height characterisation from scanning. **a** Scan cleaning process **b** burr profiles extraction **c** burr height calculation and **d** graphical representation of burr accumulation

accumulation. The accumulated cut thickness of a pass is defined as the sum of the cut thickness of all the previous cuts and of the current one. The error bars represent plus and minus 1.96 times the standard deviation. They do not take into account directly the measurement uncertainty of the LASER profilometer but represent the variability of the burr height calculation from the 3D scan. The device measurements uncertainties are considered to be of an inferior order.

On a large majority of the scans, the burr is homogeneous all along the sample exit edge. The few samples where it is not the case are not taken into account in the following discussions. The problem is linked to the difficulty to produce sharp edges during the samples manufacturing, and not to material heterogeneity like Régnier et al. observed in [1].

The machining parameters used during this study are presented in Table 1.

Four sample geometries presented on Fig. 5 have been designed to provide six various exit plane orientations. Indeed, the geometries 1 and 4 on Fig. 5 can be reversed in the tool holder to change the exit plane orientation. Φ_{ep} and Φ_{es} are respectively the principle and secondary exit angles, defined on side and top view of the sample. This two angles control the exit plane orientation. Φ_{ep} is equal to Φ_e in Fig. 2,

Table 1 Machining parameters used for the experiments

Parameters	Level
Normal rake angle (γ_n)	2°; 8°; 14°
Cutting edge inclination angle (λ_s)	0°; 5°; 10°
Cut thickness (h)	10 µm; 30 µm; 50 µm
Cutting edge radius (r_β)	10 µm; 30 µm
Cutting tool material	High-speed steel

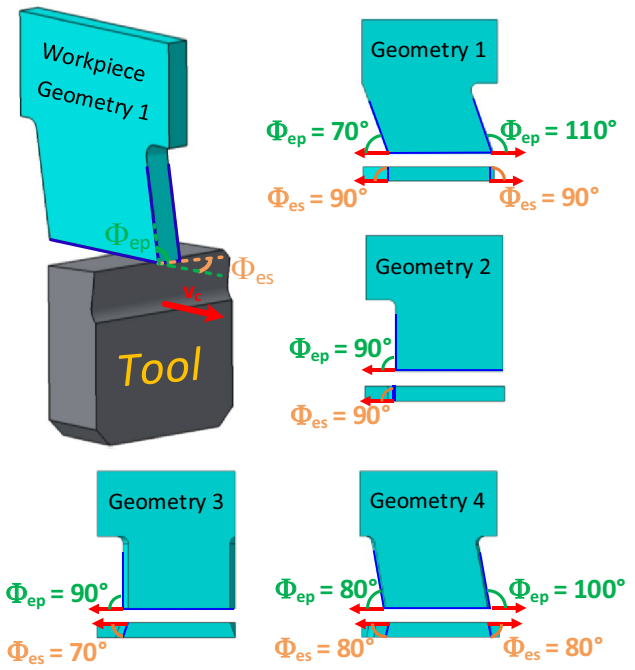

Fig. 5 Four sample designs leading to six different exit plane orientations: (Φ_{ep}=70°, Φ_{es}=90°), (Φ_{ep}=80°, Φ_{es}=80°), (Φ_{ep}=90°, Φ_{es}=90°), (Φ_{ep}=90°, Φ_{es}=70°), (Φ_{ep}=100°, Φ_{es}=80°), (Φ_{ep}=110°, Φ_{es}=90°)

relating to the state of the art. Thus, the principle exit angle changes from 70 to 110° and the secondary from 70 to 90°.

Each presented experiment started from new samples. The test designations used in this article are the following ones: (γ_n(°), (λ_s°))_h(µm)_r_β(µm)_ Φ_{ep}(°)_Φ_{es}(°).

2.2 Analysis of parameters effect on burr height accumulation

Thirty-one experiments of burr accumulation were conducted at the cutting speed of 2 m/min. Each one includes numerous cuts, e.g., one hundred for some with a cut thickness equals to 10 µm. First observations show that the burrs are homogeneous along the sample exit edge and their height is constant after each cut. The burr matter is not push in a particular area of the sample exit edge even if the cutting edge inclination angle (λ_s) is not equal to 0° or the secondary exit angle is different of 90°.

Figure 6 shows experimental curves of burr height evolution as a function of the accumulated cut thickness. Three zones are observed (cf. Fig. 6a). Starting from low to high accumulated cut thickness, the 1st one corresponds to a significant increase of the height after each pass, which is followed by the 2nd zone corresponding to a threshold. During the 3rd one, the height increases again but with a lower rate compared to what could be observed during the 1st zone.

Figure 6a shows that for a same principle exit angle, the cut thickness (h) has the greatest influence on the burr height. Its increase from 10 to 50 µm leads to a burr height rise. The change of cutting geometry with rake angles (γ_n) between 2 and 14° and cutting edge inclination angles between 0 and 10° have only little influence. The variation of the cutting edge radius (r_β) from 10 to 30 µm has no significant influence.

The increase of the principle exit angle induces a rise of burr height, as shown on Fig. 6b. The configurations where the principle exit angles are 80° and 100° also have a secondary exit angle of 80°, not 90° as the other ones. Experiments with a Φ_{ep} angle equals to 70° and a 30 µm or 50 µm cut thickness have been conducted, but are not represented. Indeed, it leads to burrs with chamfer and no measurable burr height.

Figure 6c introduces the influence of the secondary burr exit angle with samples having a principle exit angle of 90°. This parameter seems to have an influence here. However, it is also observed that the curves of the samples with a secondary exit angle of 90° have a delay before starting. After inspections, these samples have an unwilling small chamfer at the exit edge resulting locally in a decrease of the principle exit angle to a value lower than 90°. The cut thickness being smaller than these chamfers height that certainly has an influence on the burr height by changing the local exit angle. This phenomenon may also explain the differences of the curves at greater accumulated cut thickness and prevent from giving a real quantification on the effect of the secondary exit angle. Nevertheless, this effect appears to be lower than the impact of the primary exit angle. This unwilling chamfer is not as important on the other samples geometries.

The normalization is the same for all the graphics of the article.

2.3 Analysis of burr morphology during its accumulation

Figure 7 shows the bases of all the following analysis. This curve has already been presented on Fig. 6a, showing the burr height as a function of the accumulated cut thickness. The side burr pictures taken just after the various pass are matched with the curve points.

First of all, two different phases of the burr development process can be identified. The first one is linked to the two first zones of the burr height evolution and its stabilisation (cf. 2.2.). This 1st phase corresponds to the burr formation before its tip touches the sample exit free surface, and the second one starts just after. The burr grow freely only during the 1st phase which is then of great interest for the developed model presented in Sect. 3.1. On Fig. 7, the burr seems rotating while accumulating. During the 2nd phase, the burr tip touches the sample exit free surface, which explains the burr

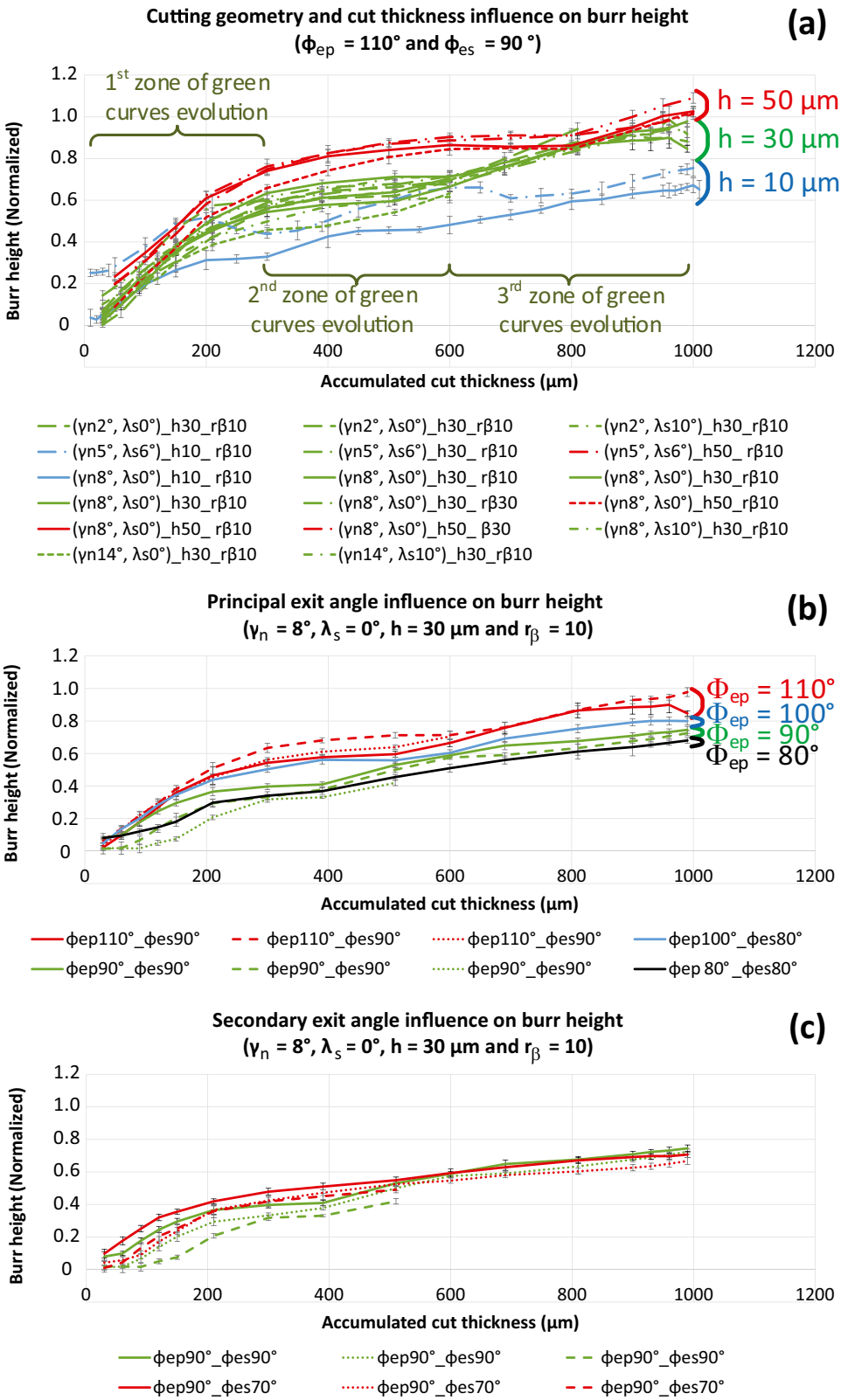

Fig. 6 Influence on burr height of **a** the cutting geometry and cut thickness, **b** principal exit angle and **c** secondary exit angle. Some configurations are repeated

height increase. Moreover, the burr seems to grow in this phase as a spiral with an initial condition corresponding to the shape of the burr at the end of the first phase.

Figure 8 shows some of the pictures of Fig. 7 during the 1st phase of burr development. The machined surface and the free exit plane of the sample are depicted with two

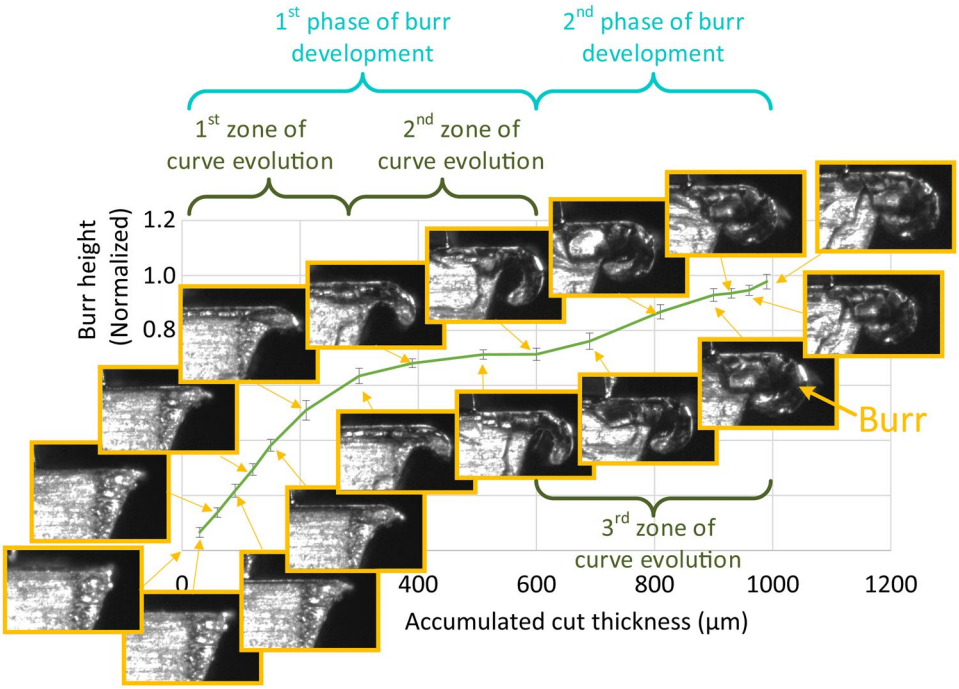

Fig. 7 Burr height evolution as a function of the accumulated cut thickness ($\gamma_n = 8°$, $\lambda_s = 0°$, $h = 30$ µm, $\Phi_{ep} = 110°$, $\Phi_{es} = 90°$)

orange lines. A third line at 20° from the exit plane is also plotted with two concentric circles. Their common centre is on the previous line. The small circle is tangent to the exit plane, the larger one is tangent to the machined surface. Their radius values are the same on all the different pictures.

It is observed that the burr rotates between the two circles as long as the burr tip does not touch the exit plane while accumulating during this multiple passes experiment.

A similar behaviour appears for all the different configurations and that explains the threshold part of the burr height

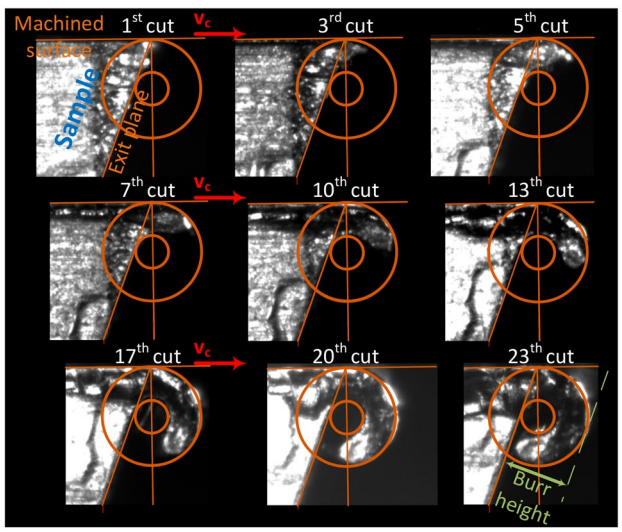

Fig. 8 In situ observation of the burr circular growth, before contact with the workpiece ($\gamma_n = 8°$, $\lambda_s = 0°$, $h = 30$ µm, $\Phi_{ep} = 110°$, $\Phi_{es} = 90°$)

curves shown on Figs. 6 and 7. This phenomenon takes place just before the burrs tips touch the samples exit planes. Burr circular growth is the base of the model presented in the next paragraph.

3 Development of a burr accumulation model before contact with the workpiece

3.1 Burr accumulation model in orthogonal cutting

In the bibliography, very few indications are given on burr accumulation at the part exit edge. The models previously presented only deal with burr formation for one cut of the tool. Nevertheless, when those methodologies are applied to describe burrs evolution after several cuts, they start rotating. Figure 9 shows the different steps that may be expected during the burr accumulation process, when the cut thickness is smaller than the burr root thickness.

Schäfer in his burr description [17] notices that a burr root radius exist, corresponding to the internal circle in Fig. 9. Régnier et al. [3] observe during a burr root accumulation experiment in a cast aluminium alloy that the curve of burr height as a function of the accumulated cut thickness (i.e. number of cut), reaches a threshold. In parallel, the images taken during the experiment show burr without chamfer rotating as the one observed in Fig. 8.

The modelling path proposed by the previews mechanical models goes from the tool tip to the plastic hinge centre and then the calculation of the burr size. The proposed model

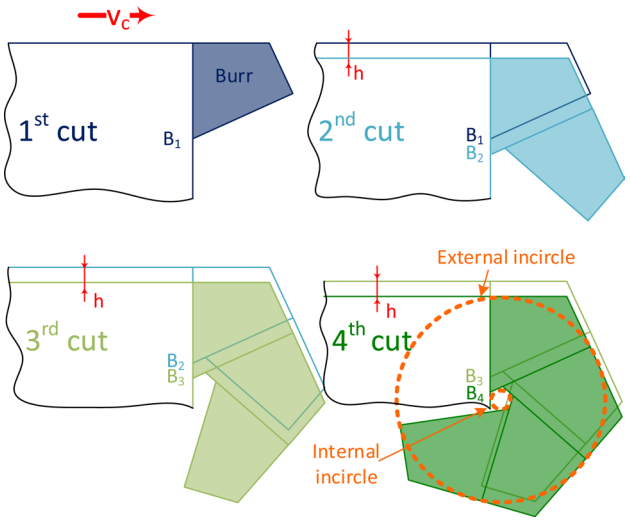

Fig. 9 Burr accumulation process expected before contact with the workpiece

in this article use a similar methodology, but on the other direction, starting from the burr heights measurements during accumulation, which gives interesting results.

The geometrical configuration of the burr accumulation model defined before the burr tip touches the exit plane is exposed on Fig. 10. The graphical representation takes place in a plane normal to the sample exit edge.

The model is composed of a large and a small circle, which are respectively tangent to the machined surface and the exit plane. Both are concentric with their centre located on a line starting from the sample exit edge and defined by an angle α with the exit plane. According to experiments, this angle is considered to be constant and equal to 20°. The experimental burr is supposed to be situated between both circles. ψ, the

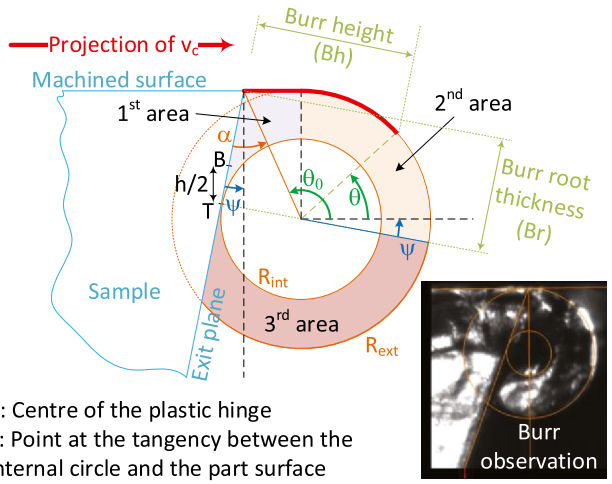

B: Centre of the plastic hinge
T: Point at the tangency between the internal circle and the part surface

Fig. 10 Geometrical model of burr accumulation before contact with the workpiece. View from a plane normal to the part exit edge

local exit angle, is the angle between the exit plane and the line normal to the machined surface. The positive direction is considered anti-clockwise. The ψ angle is linked with the principle and secondary exit angles by the formula (1). This equation results from the dot product of the normal vector of the exit plane and the normal vector of the machined surface.

$$\Psi = \arccos\left[\frac{\cos(\Phi_{ep}).\sin(\phi_{es})}{\sqrt{sin^2(\Phi_{ep}) + cos^2(\phi_{ep}).sin2(\phi_{es})}}\right] - \frac{\pi}{2} \quad (1)$$

The θ angle is the parameter that drives the burr tip location. Three different areas are identified as follows:

$$\begin{cases} 1^{st}area & if\theta > \frac{\pi}{2} \\ 2^{nd}area & if\frac{\pi}{2} \geq \theta \geq -\Psi \\ 3^{rd}area & if -\Psi > \theta \end{cases} \quad (2)$$

Inside the 2nd area, the burr is contained between the two circles and the burr height increases when θ decreases. The third area corresponds to the situation when θ may change but the burr height has reached a threshold and does not change anymore. The 1st area is the 1st stage of the burr growth where the volume of burr added by each cut is a function of θ. However, considering the values of the ψ and α angles during the conducted experiments, the size of this 1st area is considered negligible compared to the ones of the 2nd and 3rd area. According to the observations, this 1st area is filled after one or two cuts (cf. Fig. 8). The 1st zone of the curves evolution (cf. 2.2) corresponds to the 1st and 2nd area of the model. The 2nd zone of the curves (the threshold) is linked to the 3rd area.

For simplification purpose, the modelled burr is considered to be the red curve on Fig. 10, following a straight line in the 1st area of the model, and then the external circle in the 2nd and 3rd areas.

By construction, the internal circle radius depends on the external circle one, by the following formula:

$$R_{int} = R_{ext}.\frac{\sin(\alpha)}{\cos(\alpha - \Psi)} \quad (3)$$

The volume of matter added to the burr, after each cut, is considered to be constant (the 1st area of the model being neglected). This implies that the parameter θ can be described by a linear function with respect to the cut number (C_n):

$$\theta = \Delta\theta_{/cut}.C_n + \theta_0 + \varepsilon \quad (4)$$

ε allows adapting the small variation of the samples geometry due to their manufacturing. The θ_0 angle is equal to the following:

$$\theta_0 = \frac{\pi}{2} + \alpha - \Psi \quad (5)$$

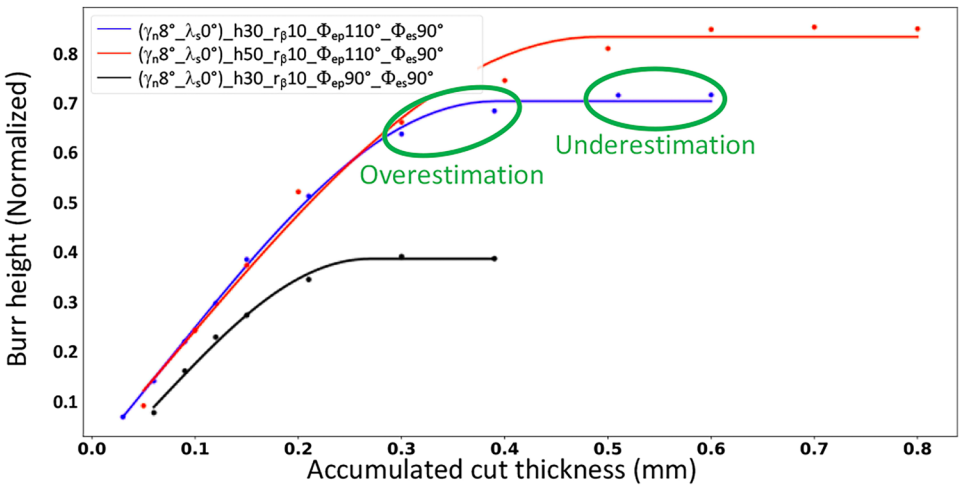

Fig. 11 Three burr height evolutions with the modelled curves identified by best-fit methodology

The burr model is defined with five coefficients. α and ψ are inputs but $\Delta\theta_{/\text{cut}}$, R_{ext} and ε need to be identified thanks to a best-fit algorithm on experimental curves (presented in paragraph 3.2).

Burr height (Bh) can then be calculated by the following:

$$\begin{cases} B_h = R_{\text{ext}}.[\left(\cos\left(\frac{\pi}{2}+\Psi\right)+\frac{\sin(\alpha)}{\cos(\alpha-\Psi)}\right)-\tan\left(\theta-\frac{\pi}{2}\right).\cos(\Psi)] & if\,\theta > \frac{\pi}{2} \\ B_h = R_{\text{ext}}.(\cos(\theta+\Psi)+\frac{\sin(\alpha)}{\cos(\alpha-\Psi)}) & if\,\frac{\pi}{2} \geq \theta \geq -\Psi \\ B_h = R_{\text{ext}}.(1+\frac{\sin(\alpha)}{\cos(\alpha-\Psi)}) & if\,-\Psi > \theta \end{cases} \tag{6}$$

The location of the plastic hinge centre of the phenomenological model is situated at a vertical distance of half the cut thickness above the point (T) which is at the tangency between the exit plane and the inner circle (cf. Fig. 10).

Burr root thickness (Br) can be calculated by the formula:

$$B_r = \frac{R_{\text{int}}}{\tan(\alpha)} \tag{7}$$

It is the distance taken parallel to the sample exit surface from point T to the part exit edge (cf. Fig. 10).

3.2 Identification of the burr model coefficients and their modelling

The coefficients $\Delta\theta_{/\text{cut}}$ and R_{ext} of the burr accumulation model presented in the paragraph 3.1 need to be determined. A best-fit algorithm is used to minimise the differences to the square between the measurements, corresponding to the burr heights as a function of the accumulated cut thickness, and the Bh modelled values. The ε parameter gives one additional degree of freedom and allows adjusting the starting point of the best-fit curves corresponding to the local small differences of the samples initial exit edges due to their manufacturing.

Figure 11 is an example of the results given by the algorithm, the curves are the fitted ones and the points represent the measurements. Not all of the measured points are considered, only the ones corresponding to the first phase of the burr development (cf. Fig. 7). The model underestimates the threshold value and overestimates the burr height just before, due to the facts that the burr is modelled as a line without any thickness. Actually, the burr is thick, and the tip is round, resulting in a change of location of the point used to measure the burr height after each cut (first at the tip, then on the side of the burr, cf. Fig. 8). In contrast, the point used for the burr height calculation is always the same during the first zone of the curve evolution: at the tip of the red curve on Fig. 10.

This methodology allows the determination of the different coefficients (α, ψ, $\Delta\theta_{/\text{cut}}$, ε and R_{ext}) needed for the burr accumulation model as a functions of the various experimental parameters (that could be γ_n, λ_s, r_β, h, Φ_{es}, Φ_{ep}…).

To determine the burr geometries and develop the different analyses presented in this article, the expressions for the coefficients $\Delta\theta_{/\text{cut}}$ and R_{ext} need to be modelled. The ε coefficient being only defined to adjust the small variations of the samples exit edges due to their manufacturing; it is not interesting to model it.

According to the previous discussions, h and the angle ψ are very influent on burr height. Based on experimental results, two following equations are proposed:

$$R_{ext} = \left(k_{R0} + k_{Rh}.h\right).(1 + k_{R\Psi}.\Psi) \tag{8}$$

$$\Delta\theta_{/cut} = \left(k_{\Delta 0} + k_{\Delta h}.h\right).(1 + k_{\Delta\Psi}.\Psi) \tag{9}$$

Formulations that are more complex have been tried, taking into account the cutting geometry (rake and cutting edge inclination angles), the cutting edge radius and also the

primary and secondary exit angles but the gain in accuracy is not significant. Moreover, this would imply more coefficients to identify. The proposed formulations are close to a cutting force model, as discussed in the introduction.

Twenty-eight experiments of burr accumulation (thirty-one conducted minus three leading to burr with chamfer) have been used to identify the coefficients of $\Delta\theta_{/cut}$ and R_{ext} models (Eqs. 8 and 9). Each experiment corresponds to numerous cuts. Figure 12 shows the relative error made by the two models of R_{ext} and $\Delta\theta_{/cut}$ compared to the values identified thanks to the best-fit algorithm on the twenty-eight experiments. The models residual degrees of freedom are twenty-five.

The R_{ext} model gives good results with more than 60% of experiments with modelling errors lower to 10%. The $\Delta\theta_{/cut}$ model is a little bit less reliable with around 50% of experiments with modelling errors inferior to the same limit.

3.3 Comparison to experimental results and other models

Chern and Dornfeld [14] and Toropov et al. [15] presented models to determine burr height and root thickness after one cut. Figure 13 compares the results of the burr accumulation model and the ones developed by them, on three different configurations. Burr heights on Fig. 13 are measured after one cut and burr root thicknesses after few cuts to improve the measurement accuracy. Indeed, according to the model presented in this article, *Br* is not influenced by burr accumulation.

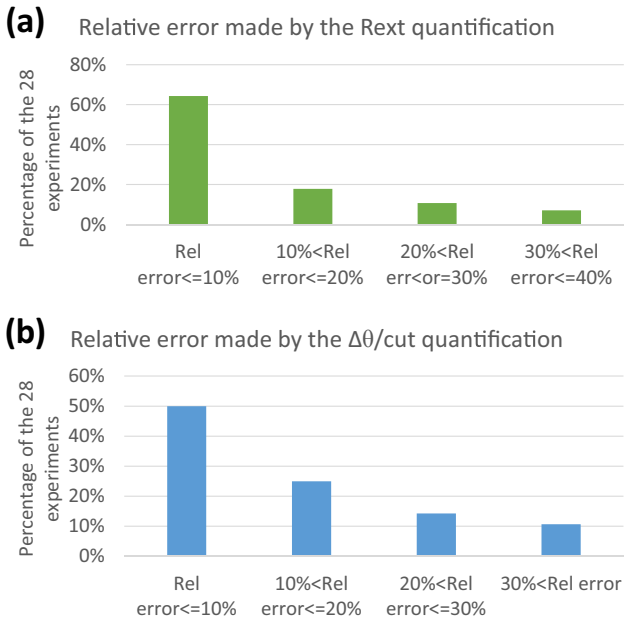

Fig. 12 Relative error (Rel error) made by the determination of **a** R_{ext} and **b** $\Delta\theta_{/cut}$

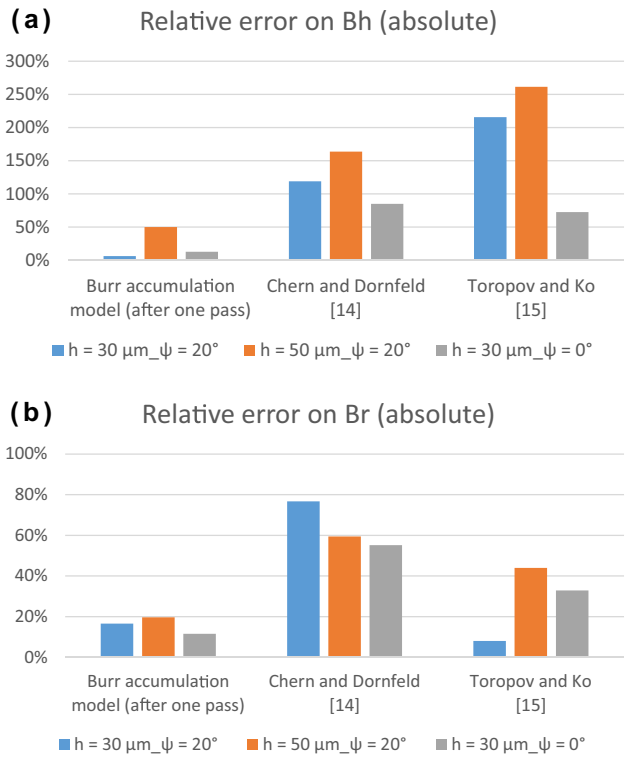

Fig. 13 Comparison after one cut of **a** the burr height and **b** the burr root thickness relative errors, for three different configurations between the presented model and the ones of [14] and [15]

However, burr height measurements after the first cuts are very dependent on the initial state of the samples and on the planing preparation process, the cut thicknesses chosen being small. By considering the entire burr growth process during accumulation, the model developed in this article is less dependent to this issue.

Burr height and root thickness calculations from the models developed in [14] and [15] have been adapted to fit the definitions presented in Fig. 2.

The burr model developed in this article gives more accurate results on burr heights and root thicknesses even after only one cut. As a reminder, burr height measurements during burr accumulation are the input of the model. There is no material behaviour assumption for these two outputs. It has to be noticed that [14] and [15] models, as explained in the introduction, are linked to burr formation in ductile materials.

4 Burr fracture determination

4.1 Quantification of the parameters needed for the estimation of burr fracture occurrence

The burr accumulation model developed in this article can directly quantify burr height, root thickness and added volume

by each cut. To estimate the fracture occurrence with some of the methodologies based on the plastic hinge presented in the introduction, the tool distance at initiation and the initial negative deformation angle have to be quantified.

The incompressibility assumption is used to determine the tool distance initiation. On Fig. 2, the area defined by the points A, C, D and E is supposed to be equal to the additional surface ($S_{/\text{cut}}$) added by each cut to the burr. Thanks to the burr accumulation model, it is determined that:

$$S_{/\text{cut}} = \pi\left(R_{\text{ext}}^2 - R_{\text{int}}^2\right).\frac{\Delta\theta_{/\text{cut}}}{2.\pi} = R_{\text{ext}}^2.\left(1 - \frac{\sin^2(\alpha)}{\cos^2(\alpha - \Psi)}\right).\frac{\Delta\theta_{/\text{cut}}}{2} \tag{10}$$

The area of ACDE is equal to:

$$A_{\text{ACDE}} = w.h - \frac{h^2}{2.\tan(\Phi)} + \frac{h^2}{2}.\tan(\Psi) \tag{11}$$

This allows the w length calculation:

$$w = \frac{S_{/\text{cut}}}{h} + \frac{h}{2.\tan(\Phi)} - \frac{h}{2}.\tan(\Psi) \tag{12}$$

The chip shear angle Φ can be determine by different methodologies; here, the next formulation has been chosen:

$$\phi = \frac{\pi}{4} - \frac{1}{2}.(arctan(\frac{F_{c,\text{cut}}.\sin(\gamma) + F_{h,\text{cut}}.\cos(\gamma)}{F_{c,\text{cut}}.\cos(\gamma) - F_{h,\text{cut}}.\sin(\gamma)}) - \gamma) \tag{13}$$

where γ is the rake angle. F_c is the cutting force along v_c and F_h the second force component along the cut thickness direction during an orthogonal experiment. The subscript "cut" means that only the forces components due to the chip contact on the rake face is taken into account (known as the "cut effect" in [18]).

Considering the negative deformation curve to be the segment AB on Fig. 2a [14], the initial negative deformation angle is as follows:

$$\beta_0 = \frac{B_r.\cos(\Psi)}{w - B_r.\sin(\Psi)} \tag{14}$$

The calculation of w and β_0 from the burr accumulation model allows using different mechanical models presented in the bibliography as shown in the next paragraph.

4.2 Crack initiation criteria

The different steps of the burr formation have been presented in the introduction. The possibility of a crack initiation and propagation along the negative deformation line to create a burr with chamfer has been mentioned. It may occur if the strain at the tool tip becomes strong enough. Different criteria for crack initiation during burr formation exist in the bibliography. The deformation during burr formation is considered to be composed of shear and bending deformation. Chern and Dornfeld [14] predict crack initiation if the equivalent strain $\overline{\varepsilon_A}$ at point A (cf. Fig. 2) is bigger than a constant ε_f. $\overline{\varepsilon_A}$ is considered to be the average of the Von Mises and Tresca equivalent strain. The calculations are as follows:

$$\overline{\varepsilon_a} = \frac{1}{2}(\frac{\gamma_A}{\sqrt{3}} + \frac{2}{3}\gamma_A) \tag{15}$$

$$\varepsilon_f = \ln(\frac{A_0}{A_f}) \tag{16}$$

$$\gamma_A \approx \cot\left(\beta_0\right) - \cot(\phi + \beta_0) \tag{17}$$

where γ_A is the shear strain on the negative shear line, at point A. A_0 and A_f are the initial and final areas of a specimen during a tensile test.

Ko and Dornfeld [19] use the variation of the deformation angle from β_0 to β when the tool moves forward for the calculation of the maximum strain $\overline{\varepsilon}_{\max}$ at the moving tool tip:

$$\overline{\varepsilon}_{\max} = \int_{\beta_0}^{\beta} \frac{\sqrt{2}}{3}.\sqrt{\frac{6}{\beta^2} + \frac{3}{2.\tan^4(\beta)}}d\beta \tag{18}$$

If $\overline{\varepsilon}_{\max}$ becomes higher to a material dependant constant, the fracture is supposed to initiate at the angle β and then propagating through point B. Thus, between the moment when the burr initiates and the fracture occurs, the burr grows a little bit.

4.3 Modelled strain and burr with chamfer occurrence

No material characterisation has been performed during this study but the different strains $\overline{\varepsilon_A}$ and $\overline{\varepsilon}_{\max}$ can be calculated for different cases in Fig. 14 (respectively a and b). It is then compared to the experimental appearance of a burr with or without chamfer, the last one corresponding to a crack propagation case. The green dots represent the configurations leading experimentally to burrs without chamfer and the orange ones to burrs with chamfer.

For comparison purpose, the integral boundary β in the calculation of $\overline{\varepsilon}_{\max}$ is chosen equal to 70°. Indeed, it is the maximum value reached when the tool is at the sample exit edge when Φ_{ep} is at an angle of 70°.

Those criteria do not succeed to estimate the occurrence of a burr with chamfer but can give an estimation. Configuration (ii), in Fig. 14c, leads to a burr without chamfer whereas (iii), with a slightly lower calculated strain, conducts to a burr with chamfer. However, it is observed that the start of the curve slope (i) in Fig. 14c is at higher rate than

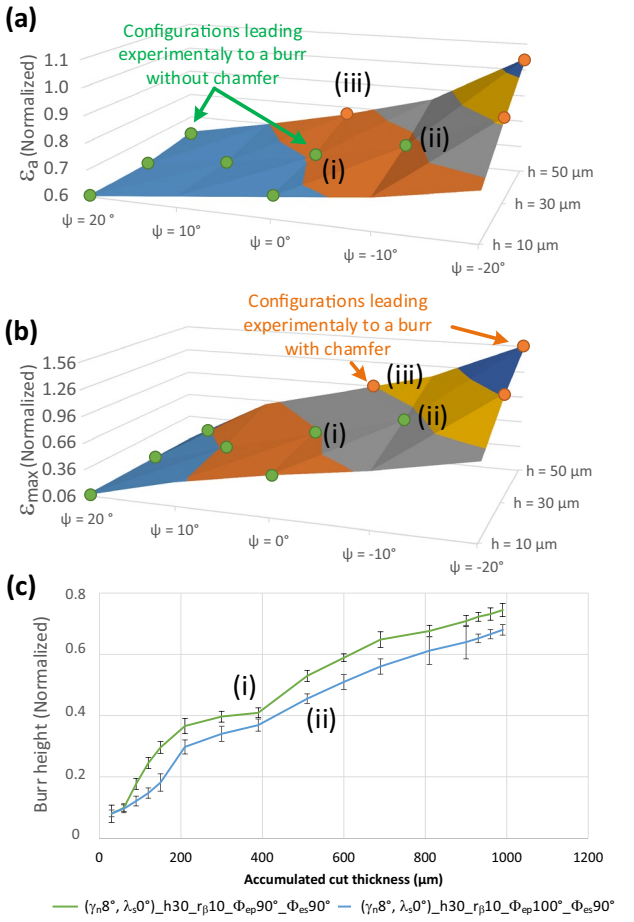

Fig. 14 Comparison of the calculated strains with the burr with chamfer occurrence, **a** $\overline{\varepsilon_A}$, **b** $\overline{\varepsilon}_{max}$. Green dots for burr without chamfer appearance and orange ones to burr with chamfer. **c** burr height evolution for configuration (i) and (ii)

the one of (ii). The second configuration may be close to a situation resulting to a burr with chamfer.

Figure 15 is a burr micrograph of a configuration leading to a burr with chamfer. The two circles of the burr accumulation

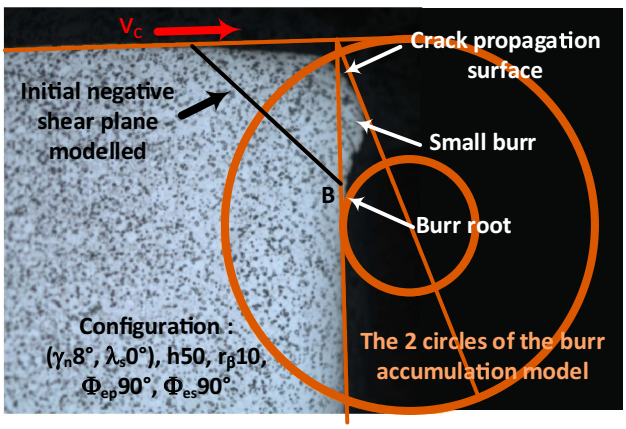

Fig. 15 Burr modelling compared to a burr without chamfer picture

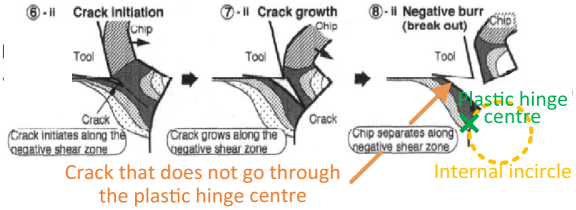

Fig. 16 Burr formation steps in case of crack initiation. Adapted from [4]

model are drawn with the calculated initial negative deformation plane. The first observation that can be made is that the modelled internal circle is tangent to the burr root, although the model coefficients have been identified on experiments that have generated burr without chamfer. The second observation is that the real crack propagation plane does not go through the burr plastic hinge centre *B*. This observation refutes the constructions of the mechanical models presented before. This can explain the difficulty for the models to evaluate if a burr with chamfer is going to initiate or not.

Hashimura et al. [4] in their observations of the burr formation steps described this phenomenon on Fig. 16. It explains why a small burr often appears at the extremity of the burr with chamfer (cf. Fig. 1). It corresponds to the burr root that initiated during the cut, just before the crack starts.

A better understanding of the crack propagation plane behaviour is needed to improve the evaluation of the conditions leading to a burr with chamfer.

5 Conclusions

This article gives a new point of view on burr formation thanks to an experiment allowing in situ burr observations and burr height measurements. Indeed, a camera and LASER profilometer located on the machine table, enable burr characterisations as closely as possible of the area of interest without any part disassembly. It allows observing the influence on burr height during accumulation of numerous machining parameters (normal rake and cutting edge inclination angles, cutting edge radius and cut thickness) and workpiece configuration (principle and secondary exit angles). Cut thickness and part exit plane inclination are the most influent parameters that can be used to reduce burr height and root thickness.

A model based on the formation of a plastic hinge has been developed without any need of material characterisation unlike the previous methodologies developed in the known literature. This model gives good results on the quantification of burr height, burr thickness and volume added to the burr by each cut. It is only based on burr height measurements during accumulation, which are simple data to obtain.

The model has been extended to determine the tool distance at initiation and the initial negative deformation angle.

This has been used to evaluate the occurrence of crack initiation leading to burr with chamfer. The methodology still needs to be improved, but it reveals the fact that the crack propagation plane does not go through the plastic hinge centre.

The rotation of the burr during accumulation appears on the observations made by Régnier et al. [3] in an aluminium alloy AlSi7Mg0.3 + 0.5Cu. An outlook to this work could be the generalisation of the present study with other workpiece materials and tool materials.

A second outlook is to apply the methodology presented in this article to three-dimensional machining operations, as milling, with higher cutting speed. Liu et al. [20] find during milling operations of a zirconium-based alloy that the increase in feed (i.e., cut thickness) results in bigger burrs, in accordance with the results in the present study. Liu et al. [20] show also that the increase in cutting speed reduces the burrs size. That may be linked to a modification of the negative shear plane by the deformation rate.

Author contribution All authors contributed to the study conception and design. Material preparation, data collection and analysis were performed mainly by Côme Legrand. The first draft of the manuscript was written by Côme Legrand, and all authors commented on previous versions of the manuscript. All authors read and approved the final manuscript.

Funding The presented study received research support from the company Safran Aircraft Engines.

Availability of data and material The data and material used are not publicly available.

Code availability The code used is not publicly available.

References

1. Régnier T, Fromentin G, Marcon B, Outeiro J, D'Acunto A, Crolet A, Grunder T (2018) Fundamental study of exit burr formation mechanisms during orthogonal cutting of AlSi aluminium alloy. J Mater Process Technol 257:112–122. https://doi.org/10.1016/j.jmatprotec.2018.02.037
2. Gillespie LK, Blotter PT (1976) The formation and properties of machining burrs. J Eng Ind 98:66–74. https://doi.org/10.1115/1.3438875
3. Régnier T, Fromentin G, Outeiro J, Marcon B, D'Acunto A, Crolet A (2016) Experimental investigation and modelling of burr formation during orthogonal cutting of A356+0.5Cu aluminium alloy. HSM. https://hal.archives-ouvertes.fr/hal-01598609
4. Hashimura M, Chang YP, Dornfeld DA (1999) Analysis of burr formation mechanism in orthogonal cutting. J Manuf Sci Eng 121:1–7. https://doi.org/10.1115/1.2830569
5. Régnier T, Fromentin G, D'Acunto A, Outeiro J, Marcon B, Crolet A (2018) Phenomenological study of multivariable effects on exit burr criteria during orthogonal cutting of AlSi alloys using principal components analysis. J Manuf Sci Eng 140:101006. https://doi.org/10.1115/1.4040623
6. Olvera O, Barrow G (1996) An experimental study of burr formation in square shoulder face milling. Int J Mach Tools Manuf 36:1005–1020. https://doi.org/10.1016/0890-6955(96)00014-4
7. Aurich JC, Dornfeld D, Arrazola PJ, Franke V, Leitz L, Min S (2014) Burrs—analysis, control and removal. CIRP Ann 58:519–542. https://doi.org/10.1016/j.cirp.2009.09.004
8. Niknam SA, Songmene V (2014) Analytical modelling of slot milling exit burr size. Int J Adv Manuf Technol 73:421–432. https://doi.org/10.1007/s00170-014-5758-y
9. Bourlet C, Fromentin G, Harika E, Crolet A (2016) Analysis and modeling of burr formation during the plane milling of cast aluminum alloy using polycrystalline diamond tools. J Manuf Sci Eng 138:081010. https://doi.org/10.1115/1.4032584
10. Régnier T (2018) Experimental analysis and burr formation modeling in the AlSi7Mg0.3+0.5Cu alloy – Application to orthogonal cutting and milling. PhD Thesis. https://pastel.archives-ouvertes.fr/tel-02049734
11. Ko S-L, Dornfeld DA (1991) A study on burr formation mechanism. J Eng Mater Technol 11375–11387. https://doi.org/10.1115/1.2903385
12. Pekelharing AJ (1980) Cutting tool damage in interrupted cutting. Wear 62:37–48. https://doi.org/10.1016/0043-1648(80)90035-6
13. Ko S-L, Dornfeld DA (1994) Burr formation and fracture in oblique cutting. J Mater Process Technol 62:24–36. https://doi.org/10.1016/0924-0136(95)02125-6
14. Chern G-L, Dornfeld DA (1996) Burr/breakout model development and experimental verification. J Eng Mater Technol 118:201–206. https://doi.org/10.1115/1.2804887
15. Toropov AA, Ko SL, Lee JM (2013) A new burr formation model for orthogonal cutting of ductile materials. CIRP Ann 55:55–58. https://doi.org/10.1016/S0007-8506(07)60365-5
16. Niknam SA, Songmene V (2013) Modeling of burr thickness in milling of ductile materials. Int J Adv Manuf Technol 66:2029–2039. https://doi.org/10.1007/s00170-012-4479-3
17. Schäfer F (1975) Entgraten: Theorie, Verfahren. Krausskopf-Verlag, Anlagen
18. Altintas Y (2000) Metal cutting mechanics, machine tool vibrations, and CNC design. Cambridge University Press
19. Ko S-L, Dornfeld DA (1996) Analysis of fracture in burr formation at the exit stage of metal cutting. J Mater Process Technol 58:189–200. https://doi.org/10.1016/0924-0136(95)02124-8
20. Liu Y, Gong Y, Liu W, Xu L, Sun X (2020) Experimental investigations on flank contour accuracy of milling groove for Zr-based bulk metallic glass using mesoscale milling. Int J Adv Manuf Technol 108:785–799. https://doi.org/10.1007/s00170-020-05464-x